A Four-Dimensional Survey of the Almeria–Oran Front by Underwater Gliders: Tracers and Circulation

DANIEL L. RUDNICK,[a] NIKOLAOS D. ZAROKANELLOS,[b] AND JOAQUIN TINTORÉ[b,c]

[a] *Scripps Institution of Oceanography, La Jolla, California*
[b] *Balearic Islands Coastal Observing and Forecasting System (SOCIB), Palma de Mallorca, Spain*
[c] *IMEDEA (CSIC-UIB), Esporles, Spain*

ABSTRACT: A four-dimensional survey by a fleet of seven underwater gliders was used to identify pathways of subduction at the Almeria–Oran Front in the western Mediterranean Sea. The combined glider fleet covered nearly 9000 km over ground while doing over 2500 dives to as deep as 700 m. The gliders had sensors to measure temperature, salinity, velocity, chlorophyll fluorescence, and acoustic backscatter. Data from the gliders were analyzed through objective maps that were functions of across-front distance, alongfront distance, and time on vertical levels separated by 10 m. Geostrophic velocity was inferred using a variational approach, and the quasigeostrophic omega equation was solved for vertical and ageostrophic horizontal velocities. Peak downward vertical velocities were near 25 m day^{-1} in an event that propagated in the direction of the frontal jet. An examination of an isopycnal surface that outcropped as the front formed showed consistency between the movement of the tracers and the inferred vertical velocity. The vertical velocity tended to be downward on the dense side of the front and upward on the light side so as to flatten the front in the manner of a baroclinic instability. The resulting heat flux approached 80 W m^{-2} near 100-m depth with a structure that would cause restratification of the front. One glider was used to track an isotherm over a day for a direct measure of vertical velocity as large as 50 m day^{-1}, with a net downward displacement of 15 m over the day.

KEYWORDS: Ocean; Mediterranean Sea; Ageostrophic circulations; Vertical motion; Fronts; Tracers

1. Introduction

The study of the distribution of tracers and circulation surrounding fronts has been active for decades. The notion that fronts are sites of strong vertical flow in the atmosphere dates back at least to the work of Bergeron (1937). Niller and Reynolds (1984) offers an early example of using ship surveys and drifters to infer three-dimensional circulation at an oceanic front, including a remarkable demonstration of increasingly fine horizontal structure observed by surveys with better resolution repeated in the same area over the years. At mesoscale horizontal scales larger than about 10 km and at subinertial frequencies, the ocean tends to be in geostrophic balance. The breaking of the geostrophic balance may lead to ageostrophic vertical and across-front circulations, in a broad class of phenomena now referred to as the submesoscale (McWilliams 2016; Mahadevan 2016). The vertical circulation at fronts is important to biological processes as upwelling brings nutrients into the euphotic zone enhancing primary productivity, and downwelling takes the resulting maxima below the euphotic zone where the highs in such quantities as chlorophyll concentration may be a useful tracer (Mahadevan 2016). A central goal of this work is to quantify the pathways by which surface water reaches the deeper ocean using physical and biological tracers and inferences of the ageostrophic circulation.

The approximation that alongfront flow is in geostrophic balance was used by Sawyer (1956) to derive a diagnostic equation governing the ageostrophic vertical and across-front circulation. This early version of the omega equation (Hoskins et al. 1978) led to many studies to diagnose vertical circulations in the atmosphere. Application of the omega equation to the ocean was spurred by the evolution of observing technology to achieve rapid mesoscale resolving ship surveys (Tintoré et al. 1991; Pollard and Regier 1992; Rudnick 1996; Allen and Smeed 1996; Viúdez et al. 1996a). Such a survey using a towed device carrying a conductivity–temperature–depth (CTD) instrument and a shipboard acoustic Doppler current profiler (ADCP) took a few days to complete and demands on ship time often meant that only a few such surveys were possible (Rudnick and Luyten 1996).

Underwater gliders have seen increased use for ocean surveys at relatively fine, 10 km and less, horizontal resolution (Rudnick 2016). In typical use, an underwater glider may dive from the surface to 1000 m and back, completing the cycle in 6 h while covering 6 km. This horizontal resolution raises the possibility that gliders can be useful for fine resolution surveys. The main limitation of gliders is their relatively slow horizontal speed of roughly 0.25 m s^{-1} as compared with the survey speed of a ship towing a SeaSoar profiling vehicle (Pollard 1986) of about 4 m s^{-1} (Rudnick and Cole 2011). This limitation may be overcome by using a fleet of gliders. For example, a fleet of eight gliders would have a cumulative

---

Corresponding author: Daniel L. Rudnick, drudnick@ucsd.edu

survey speed of about 2 m s^{-1}, comparable to the speed of a ship using an Underway CTD profiler (Rudnick and Klinke 2007) in tow-yo mode (Tandon et al. 2016). The chief advantage of a glider fleet is persistence as it may be on site for months surveying continuously, while the community demands on research vessel time usually prevent such an intensive use of a ship. Another potential benefit of a fleet of gliders is that the observations may be more broadly distributed over the survey area during a short time interval.

In this work, we used a fleet of seven underwater gliders to survey the Almeria–Oran (AO) Front over a period of 2 months in March–May 2019. The AO Front is readily apparent in salinity as a boundary between salty Mediterranean water to the east and relatively fresh water of Atlantic origin to the west (Tintoré et al. 1988). The circulation in the Alboran Sea is topographically constrained, as the inflow from the Atlantic traverses two gyres, the Western Alboran Gyre and the Eastern Alboran Gyre (Arnone et al. 1990). These gyres are often present, but they can vary in strength throughout the year (Renault et al. 2012; Macias et al. 2016) and are affected by local wind (Macías et al. 2008). The AO Front is located at the eastern edge of the Eastern Alboran Gyre. Because the AO Front is topographically locked and easily located by its salinity signal, it has previously been the site of experiments focusing on frontal circulation (Allen et al. 2001a). The AO Front was chosen as a site for the Coherent Lagrangian Pathways from the Surface Ocean to Interior (CALYPSO; Mahadevan et al. 2020) project to which this work is a contribution. Pilot work at the AO using underwater gliders was done during May–August 2018 (Zarokanellos et al. 2022; Garcia-Jove et al. 2022).

An outline of the paper is as follows. In section 2 the dataset created by the glider fleet is described. Analyses of these data are presented in section 3, including objective maps of all measured variables, the estimation of geostrophic currents, a solution of the quasigeostrophic (QG) omega equation, and the calculation of potential vorticity. The exposition of results in section 4 includes the distribution of physical and biological tracers, a comparison of observed and geostrophic currents, an examination of the inferred vertical velocity, and a direct measure of vertical velocity. A central result is the observation of a downwelling event at the AO Front. The paper closes with a discussion and conclusions in section 5 and 6, respectively.

2. Data

A fleet of underwater gliders was deployed toward an overarching goal of resolving the structure of the AO Front. The complete fleet of seven gliders included six Spray (Rudnick et al. 2016; Sherman et al. 2001) gliders and one Slocum (Schofield et al. 2007). The Spray gliders were equipped with CTDs to measure pressure, temperature, and salinity, ADCPs to measure velocity and acoustic backscatter at 1 MHz, and chlorophyll fluorometers. The Slocum had sensors to measure dissolved oxygen and turbidity in addition to a CTD and fluorometer but did not have an ADCP. The Spray gliders were deployed (Fig. 1) for the period 20 March–20 May 2019 and
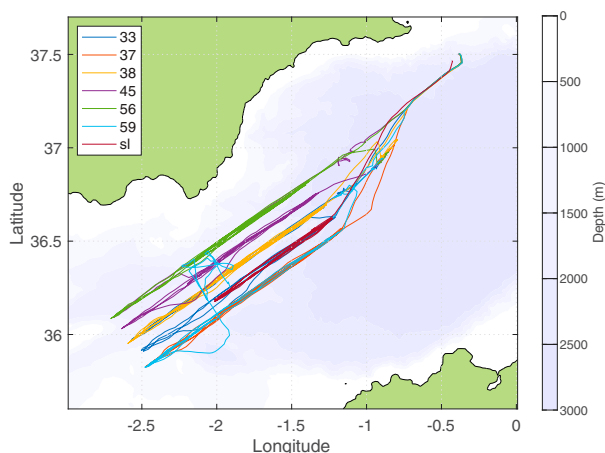

Fig. 1. Underwater glider tracks for the period 20 Mar 2019–20 May 2019. Serial numbers of the Spray gliders are indicated in the legend, with the Slocum designated by "sl."

covered 8334 km over ground while doing 2309 dives to as deep as 700 m. The Slocum was deployed for the period 20 March–14 April and covered 607 km over ground while doing 251 dives. Considering that the speed of gliders was 0.26 m s^{-1}, the fleet of seven gliders had a surveying capability of a ship steaming at 1.8 m s^{-1} (~3.5 kt). One of the Sprays (serial number 59) was sometimes used to drift at depth while actively tracking an isotherm. Seven drifts of 24-h duration were made for a direct measure of vertical velocity. The objective of having a four-dimensional dataset was achieved through the sampling by the glider fleet.

The glider fleet was deployed to survey in five lanes oriented to cross the AO Front (Fig. 1). The northernmost lane was positioned close to the 1000-m isobath and the southernmost lane was close to the boundary of Spain's Exclusive Economic Zone. The orientation of the array was defined by placing the central lane at an origin of 36.232°N, 2.091°W with the along-lane direction toward 36.696°N, 1.265°W for a heading of 55.1°. Our operational definition of across front was thus the direction along lanes, and alongfront was the direction across lanes. We use this definition henceforth in describing alongfront and across-front flow. The lanes were separated in the across-lane direction by 8.75 km so that the five lanes spanned 35 km. The length of the lanes was adjusted during the experiment to span 145 km (Fig. 2). A glider was able to complete the full length of a lane in about 6.5 days. A dive to 700 m was typically completed in 4 h, during which time the glider traveled 4 km. The gliders were purposely piloted so that there were gliders on either side of the observed region, thus filling up the phase space of across-front distance and time (Fig. 2). The glider fleet produced a total of over 60 sections toward the goal of resolving the structure of the AO Front.

Data processing included quality control and postdeployment calibration. Navigational data from the GPS were subjected to an automatic quality control algorithm to identify bad values of time, latitude, and longitude, followed by a manual examination. Bad navigational data were replaced by
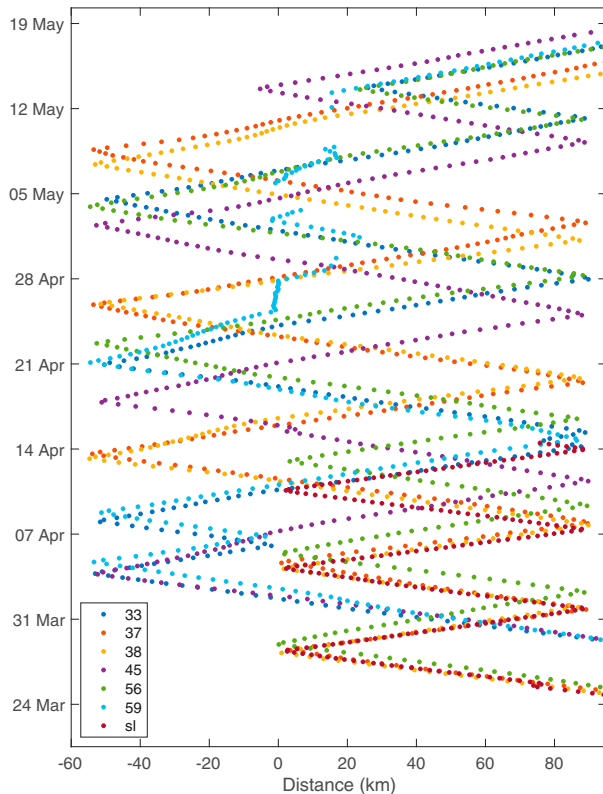
FIG. 2. Sampling by underwater gliders as a function of distance in the across-front direction and time, with each profile shown as a colored dot. In the legend, numbers refer to Spray glider serial numbers and "sl" indicates the Slocum glider; the colors match Fig. 1.

good values from the same surface interval. Temperature, salinity, and chlorophyll fluorescence profiles were examined manually, and bad values were flagged for exclusion. Chlorophyll fluorescence was calibrated against satellite observations with a linear correction to achieve zero values below the euphotic zone and agreement with satellite chlorophyll at the surface. The depth-average velocity was calculated using the procedures in Rudnick et al. (2018). Velocity and acoustic backscatter data from the ADCP were processed as in Todd et al. (2017), including a correction for bias in the velocity shear. All data from each profile were averaged in bins that were 10 m wide in depth over the upper 700 m. These binned data form the dataset used in all subsequent calculations.

The AO Front was not apparent in the region occupied by gliders until early April, when the front moved into the region. The front was especially strong during a period starting in mid-April shown in Fig. 3. Sections of the binned data indicate steeply sloping isopycnals extending from near the surface to greater than 100-m depth over a distance of about 50 km. Salinity was a clear marker of the front with relatively fresh Atlantic Ocean water on the west side of the front and salty water of Mediterranean origin to the east (Fig. 3a). A surface-intensified alongfront jet reached speeds of 1 m s^{-1} near the surface and was strongly sheared across the

pycnocline (Fig. 3c). The across-front flow was slightly convergent with inflow on the west end of the section (Fig. 3d). The frontal jet strengthened as it flowed southward, with the highest velocities measured across the southernmost section (Fig. 3b). Chlorophyll fluorescence (Fig. 3f) and acoustic backscatter (Fig. 3e) served as bulk measures of phytoplankton and zooplankton, respectively. These biological tracers may provide evidence of strong downwelling when they are observed to be high below the regions where they typically grow. In the front where isopycnals sloped down from the surface, the chlorophyll fluorescence had a downward extending tongue of high values (Fig. 3f). Acoustic backscatter also showed a tongue in the same region, as well as a thin tendril of high values below 100-m depth to the east of the front (Fig. 3e). This tendril was so thin that it appeared broken in the observations, probably because the 4-km resolution of the profiles was too coarse to resolve such a thin feature. These observations suggestive of downwelling motivate the estimation of vertical velocity to follow.

3. Analyses

The observations from the glider fleet were uneven in space and time so an objective map (Bretherton et al. 1976) was used to create regularly gridded fields. For each vertical level z, an objective map was made as a function of across-front x and alongfront y position in the survey geometry and time t. The mapped variables were temperature, salinity, the two horizontal components of velocity, chlorophyll fluorescence, and acoustic backscatter. First, a function linear in x, y, and t was least squares fit and subtracted from the observations. The resulting anomalies were objectively mapped using a Gaussian autocovariance with e-folding scales of 13 km in x, 35 km in y, and 9 days in t. Final maps were made by summing the mapped anomalies with the linear function fit. The e-folding scales were determined by calculating the autocovariance of alongfront velocity and fitting a Gaussian function. Autocovariances of temperature, salinity, and across-front velocity were also calculated. Each variable had different e-folding scales, but the scales for alongfront velocity were representative, and for simplicity one autocovariance was used to map all variables. In the calculated autocovariances there was a large spike at zero lag representative of variability with small spatial and temporal scale. A noise-to-signal ratio of 0.4, uncorrelated between data, was used in the autocovariance to account for these energetic small scales. The resulting maps were computed on a grid 2.5 km × 2.5 km × 1 day on each 10-m vertical level. Derived variables like potential temperature, density, and potential density were then calculated from these maps. Variables were interpolated onto potential density surfaces to focus on the effects of horizontal advection. All maps were masked at an error-to-signal variance ratio of 0.3. These maps formed the input for subsequent analyses.

The next step in the analysis was to ensure that the potential density field was statically stable. Following Rudnick (1996), each vertical profile in the objective map was adjusted to be stable while minimizing the squared difference from the
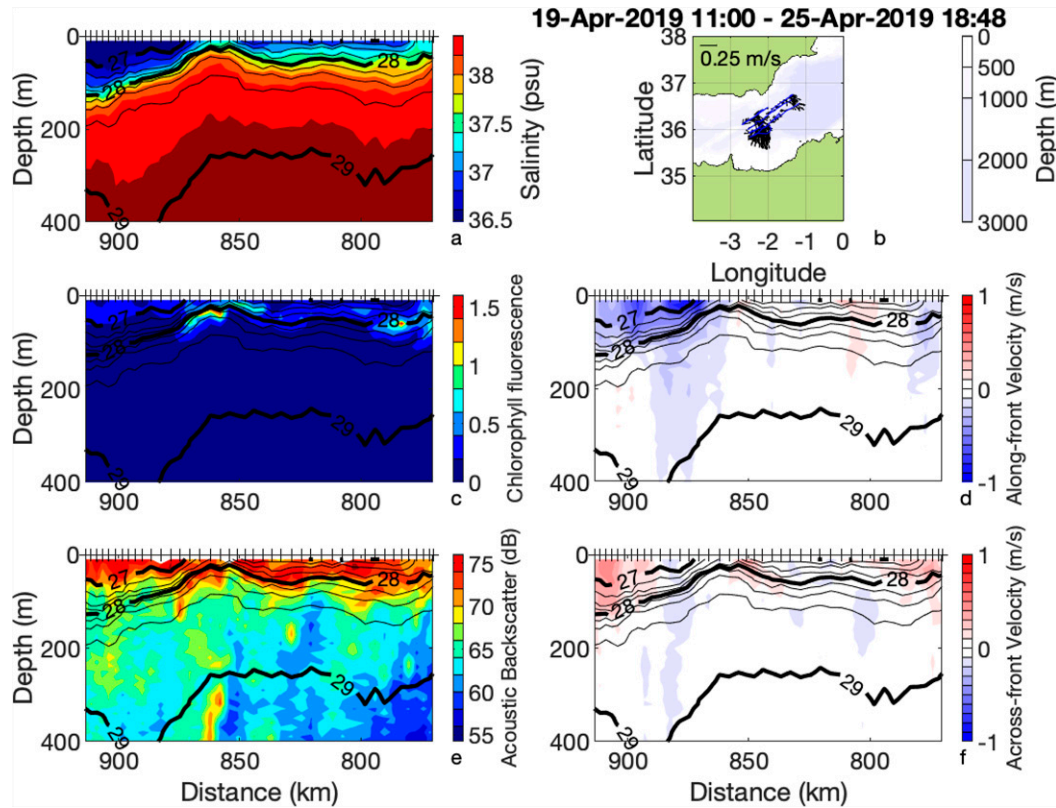
FIG. 3. Data from the glider survey during 19–25 Apr. Sections of the variables (a) salinity, (c) chlorophyll fluores-cence, (d) alongfront velocity, (e) acoustic backscatter, and (f) across-front velocity are shown from the central lane. The variables are shown in colored shading, and isopycnals are contoured in black. Distance is measured along track from the beginning of the survey. Tick marks along the upper edge of the sections show the locations of profiles. Also shown is (b) velocity averaged over the upper 700 m, depicted as vectors for all glider data during this period. The velocity scale is indicated, and bottom topography is shaded.

unadjusted profile. In practice, very few profiles had to be adjusted, and the vast majority of these were at the edges of the map where the mapping errors were highest. This stati-cally stable potential density field was used for all subsequent calculations.

The geostrophic velocity field was estimated independently for every day by finding the streamfunction that minimized the squared difference from the observed velocity field. The following description of the method follows Rudnick (1996), where additional details may be found. The geostrophic veloc-ity (u_g, v_g) may be written as

$$u_g = -\frac{\partial \psi}{\partial y} + \frac{\partial R}{\partial y} \tag{1}$$

$$v_g = \frac{\partial \psi}{\partial x} - \frac{\partial R}{\partial x}, \tag{2}$$

where $\psi(x, y)$ is a streamfunction at vertical position z_0 and

$$R = \frac{g}{f \rho_0} \int_{z_0}^{z} \rho \, dz. \tag{3}$$

Here g is gravitational acceleration, f is the Coriolis parameter, and ρ_0 is a reference density. The density ρ in the integral is poten-tial density, consistent with the QG approximation to follow. That the geostrophic velocity is horizontally nondivergent is implicit in Eqs. (1)–(3). A measure of the square difference between geo-strophic and observed velocity is the volume integral

$$\int_V \left[(u_g - u)^2 + (v_g - v)^2 \right] dV, \tag{4}$$

where the volume is defined as the upper $H = 400$ m and the horizontal extent of the objective map. Minimizing Eq. (4) with respect to variations in ψ yields the equation

$$\nabla^2 \psi = H^{-1} \left(\nabla^2 \tilde{R} + \tilde{\zeta} \right), \tag{5}$$

where ∇ is the horizontal gradient operator, the tilde notation implies vertical integration, and ζ is the vertical component of rel-ative vorticity. In solving Eq. (5) the natural boundary condition (Courant and Hilbert 1953) is used on horizontal boundaries.

The QG omega equation for the vertical velocity is diagnos-tic in the sense that there is no explicit dependence on time. The partial time derivative is eliminated by combining the
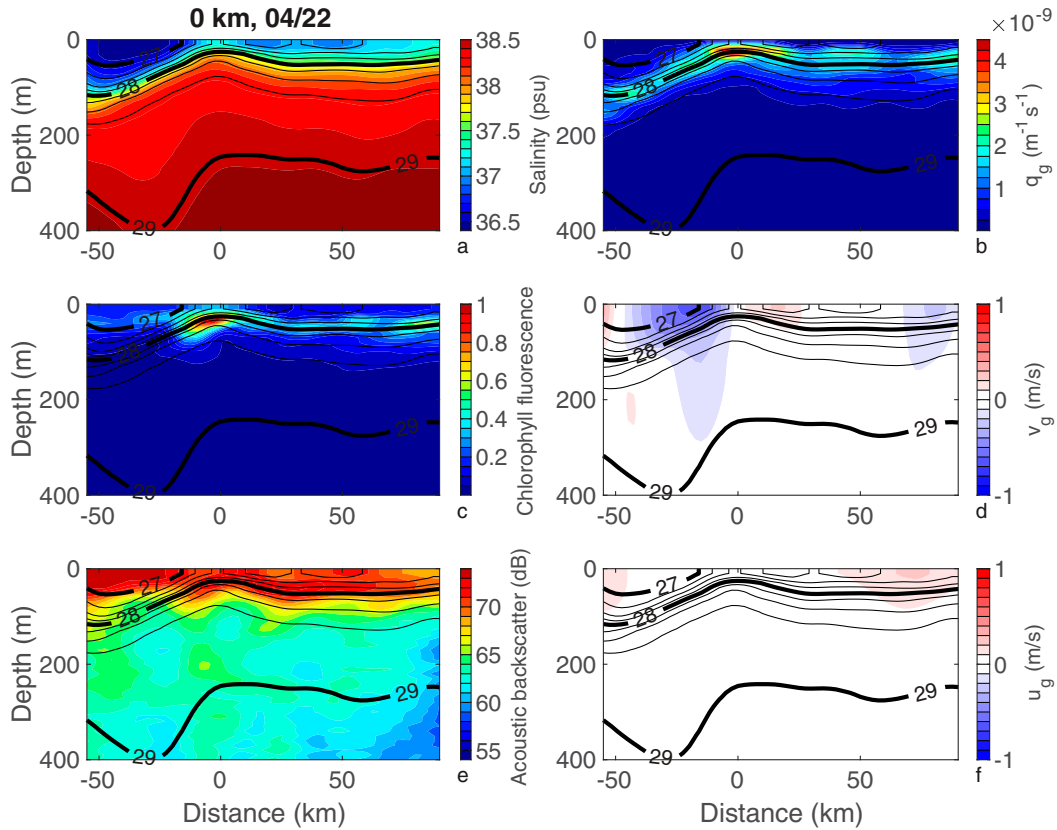
FIG. 4. Mapped variables along the central lane on 22 Apr. Sections of the variables (a) salinity, (b) geostrophic potential vorticity, (c) chlorophyll fluorescence, (d) geostrophic alongfront velocity, (e) acoustic backscatter, and (f) geostrophic across-front velocity are shown. The variables are shown in colored shading, and isopycnals are contoured in black. Distance is in the across-front x direction, and the central lane is defined to be at alongfront y position 0.

momentum and density conservation equations. The omega equation may be solved at every time step, here at the grid spacing of 1 day. The governing equations are as follows, including the horizontal momentum equations

$$\frac{D_g u_g}{Dt} - f v_a = 0 \tag{6}$$

$$\frac{D_g v_g}{Dt} + f u_a = 0, \tag{7}$$

where u_a and v_a are horizontal ageostrophic velocities and the geostrophic advection operator is

$$\frac{D_g}{Dt} = \frac{\partial}{\partial t} + u_g \frac{\partial}{\partial x} + v_g \frac{\partial}{\partial y}. \tag{8}$$

Consistent with Eqs. (1)–(3), the geostrophic velocity is given by

$$f u_g = -\frac{1}{\rho_0} \frac{\partial p}{\partial y} \tag{9}$$

$$f v_g = \frac{1}{\rho_0} \frac{\partial p}{\partial x}. \tag{10}$$

The vertical momentum equation is hydrostatic:

$$0 = -\frac{1}{\rho_0} \frac{\partial p}{\partial z} - \rho g, \tag{11}$$

where ρ is density. The equation of continuity for ageostrophic velocity is

$$\frac{\partial u_a}{\partial x} + \frac{\partial v_a}{\partial y} + \frac{\partial w}{\partial z} = 0. \tag{12}$$

The density conservation equation is

$$\frac{D_g \rho}{Dt} + w \frac{\partial \rho}{\partial z} = 0. \tag{13}$$

Taking the vertical derivative of the horizontal momentum equations and the horizontal derivatives of the density equation, summing, and using the hydrostatic equation yield the following two equations

$$\frac{\partial}{\partial x}(N^2 w) - f^2 \frac{\partial u_a}{\partial z} = 2Q_x \tag{14}$$

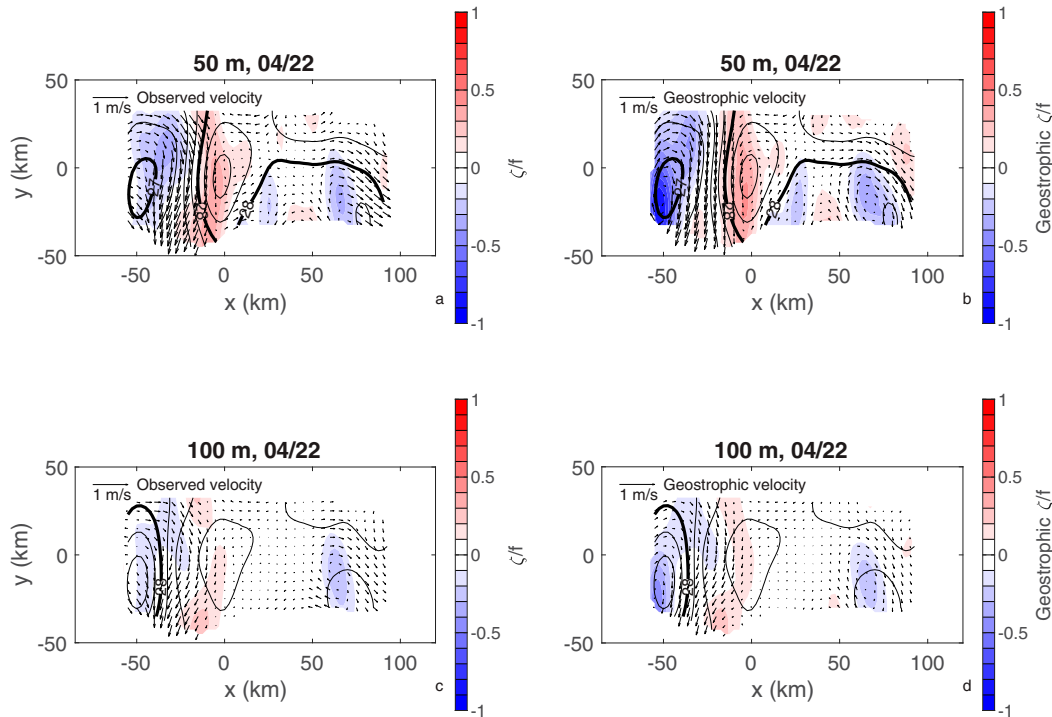$$\frac{\partial}{\partial y}(N^2 w) - f^2 \frac{\partial v_a}{\partial z} = 2Q_y, \tag{15}$$

FIG. 5. (a),(c) Observed and (b),(d) geostrophic velocity and the vertical component of relative vorticity at (top) 50 and (bottom) 100 m on 22 Apr. The vertical component of relative vorticity is normalized by the planetary vorticity f and is plotted with color shading. Horizontal velocity is indicated by arrows, with a scale in the upper-left-hand corner of the panels. Potential density is contoured with an interval of 0.25 kg m^{-3}.

where $N^2 = -(g/\rho_0)(\partial\rho/\partial z)$ is the buoyancy frequency taken here to vary in the horizontal, and the **Q** vector is

$$(Q_x, Q_y) = \frac{g}{\rho_0}\left(\frac{\partial \mathbf{u}_g}{\partial x} \cdot \nabla\rho, \frac{\partial \mathbf{u}_g}{\partial y} \cdot \nabla\rho\right). \tag{16}$$

The omega equation is found by summing the horizontal derivatives of Eqs. (14) and (15)

$$\nabla^2(N^2 w) + f^2 \frac{\partial^2 w}{\partial z^2} = 2\nabla \cdot \mathbf{Q}. \tag{17}$$

The omega equation [Eq. (17)] is solved for the vertical velocity, and Eqs. (14) and (15) are then solved to get horizontal ageostrophic velocity. In previous work the solution of Eq. (17) was often done by relaxation. Here the solution uses the sparse matrix utility in MATLAB, which has the advantage of being exact to double precision. The direct sparse solution may also entail an improvement in speed over the iterative relaxation.

Solutions of the omega equation require boundary conditions. In solving Eq. (17), vertical velocity is set to zero at the boundaries. Setting w to zero at the surface is appropriate, the lateral boundaries have little effect on the solution in the interior of the observed region, but the bottom boundary can have a strong influence on velocities inferred from the omega equation. We have observations consistently down to 700 m and we are interested in the solution

in the upper 400 m. We set the lower boundary at 2100 m, near the depth of the ocean bottom in the region, and take **Q** and N to be zero below 700 m. As a measure of sensitivity, we solved Eq. (17) using a lower boundary at 1400 m and found that there was negligible change in the resulting w in the upper 400 m when compared with solutions with a lower boundary at 2100 m. This approach of moving the bottom boundary deeper than the observed region follows Rudnick (1996). Pietri et al. (2021) addressed the bottom boundary condition in the solution of the omega equation using data from a numerical model applied to several different locations, concluding that "the use of a buffer region to increase the domain depth following Rudnick (1996) can ameliorate the reconstruction skill and provide an optimum over all possible choices but the improvement is generally marginal." We tend to agree with this conclusion of Pietri et al. (2021). The solution of Eqs. (14) and (15) for horizontal ageostrophic velocity is achieved by vertical integration using a bottom boundary condition of zero velocity.

The dynamical tracer potential vorticity is often used to diagnose frontal circulation. Here we calculate the potential vorticity q defined as

$$q = -\frac{1}{\rho_0}\left[(f + \zeta)\frac{\partial\rho}{\partial z} - \frac{\partial v}{\partial z}\frac{\partial\rho}{\partial x} + \frac{\partial u}{\partial z}\frac{\partial\rho}{\partial y}\right], \tag{18}$$
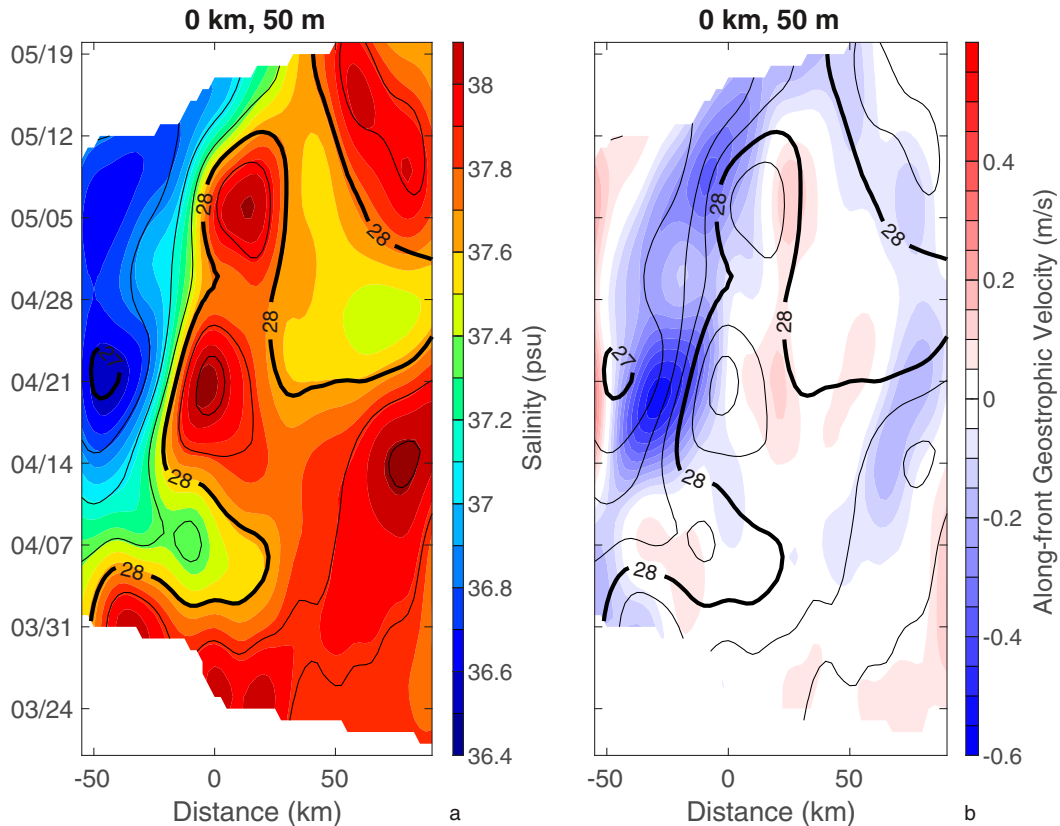
where

FIG. 6. (a) Salinity and (b) geostrophic alongfront velocity on the central lane at 50 m as a function of across-front distance and time. Potential density is contoured with an interval of 0.25 kg m^{-3}. The front appeared during the second week of April and intensified over the next week.

$$\zeta = \frac{\partial v}{\partial x} - \frac{\partial u}{\partial y} \qquad (19)$$

is the vertical component of relative vorticity. In the following we consider potential vorticity calculated from the observed velocity ζ and from the geostrophic velocity ζ_g. The tracers available for diagnosing circulation include salinity, chlorophyll fluorescence, and acoustic backscatter in addition to potential vorticity. These tracers are interpolated onto potential density surfaces to enable this diagnosis.

4. Results

The results of the objective map are four-dimensional fields of the observed variables. As an example of the resulting fields consider the mapped section along the central lane at a time near the midpoint of the section shown previously. This mapped section (Fig. 4) shows a strong fidelity to the raw observations (Fig. 3), with the effect of smoothing apparent. The structure of the salinity and potential density front is retained (Fig. 4a), with some of the finer-scale fluctuations (perhaps caused by internal waves) damped by the smoothing. The high in chlorophyll fluorescence on the plunging isopycnal is evident (Fig. 4c) although the feature is thicker in the

objective map. The very fine tendrils in observed acoustic backscatter (Fig. 3e) are not represented in the objective map (Fig. 4e). In general, the objective map provides a faithful representation of the observed fields on the mapped length scales.

The focus here is on the geostrophic velocity fields as they are the forcing for the omega equation, and they tend to filter out the effects of unresolved motions due to internal waves. The alongfront velocity jet (Fig. 4d) is strong in the map, including a tendency for the cyclonic side to be sharper. The across-front velocity (Fig. 4f) is relatively weak and some of the finer-scale fluctuations in the observations (Fig. 3f) are filtered out. The geostrophic potential vorticity (Fig. 4b) is maximum in the high stratification region at the base of the mixed layer. The highest value of q_g is found in the region of cyclonic vorticity on the dense side of the front. In regions with deeper mixed layers subduction may be suggested by a tongue of low q_g descending along the sloping front (Rudnick and Luyten 1996). This kind of low q_g feature is not observed in these observations of the AO Front with a relatively thin mixed layer.

An examination of observed and geostrophic velocity and vorticity helps to understand the horizontal circulation and the effects of the geostrophic constraint (Fig. 5). The dominant feature of the flow is the alongfront jet that is mostly
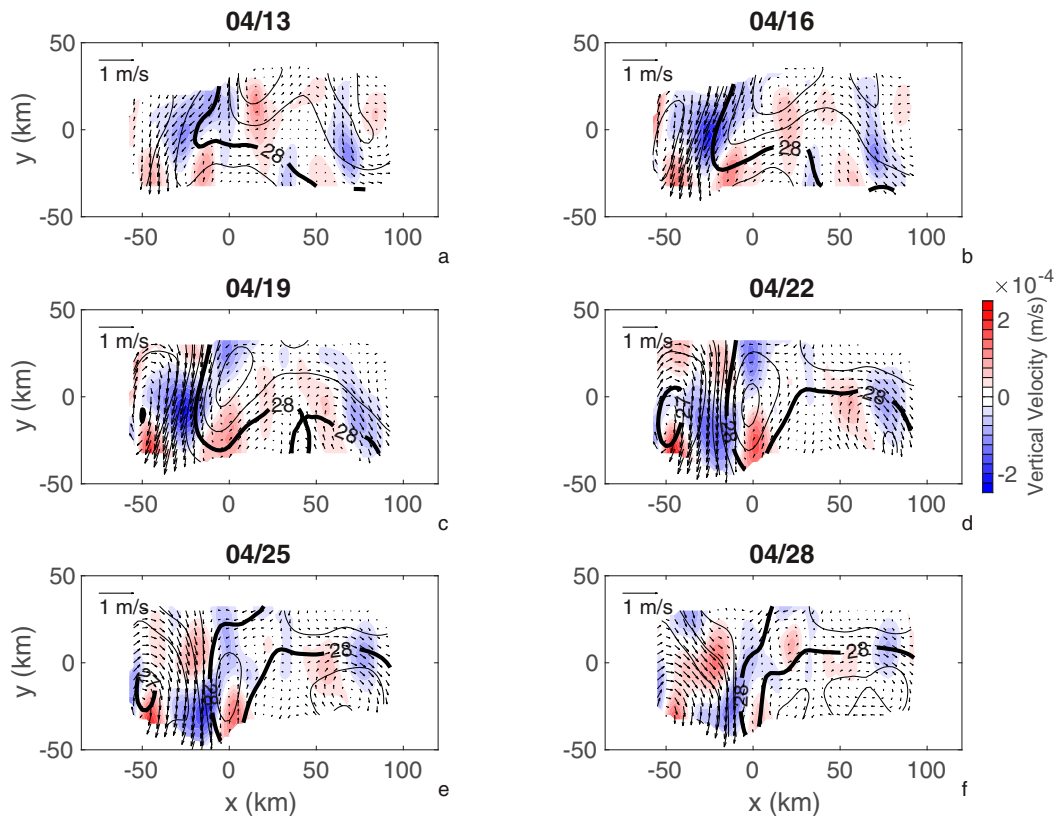
FIG. 7. Vertical velocity at 50 m at 3-day intervals in the period 13–28 Apr as a function of across-front distance x and alongfront distance y. Vertical velocity is shown with color shading, potential density is contoured with an interval of 0.25 kg m^{-3}, and geostrophic horizontal velocity is shown using vectors, with a scale in the upper-left corner of each panel. Note the co-occurrence of the region with the sharpest gradient in potential density, the strongest frontal jet, and the largest downwelling.

parallel to isopycnals. Even with the geostrophic constraint, it is the vertical shear of horizontal velocity that must align with potential density, so that velocity may cross isopycnals. This tendency of velocity to cross isopycnals is important because it is what allows a vertical velocity in the QG approximation as in the density equation [Eq. (13)]. The vertical component of relative vorticity ζ normalized by the planetary vorticity f has extrema on either side of the frontal jet. On the cyclonic side of the jet at 50-m depth, these extrema peak at nearly 0.5 in both observed and geostrophic fields. The jet and its associated vorticity weaken with depth until typical values of ζ/f are a few tenths at 100-m depth. There is a notable difference at 50-m depth between the observed and geostrophic vorticities on the anticyclonic side of the front near the edge of the map where the geostrophic ζ/f approaches -1. At this location, the observed flow is strongly across isopycnals while the geostrophic flow circulates around a region of less dense water. Because this region is near the boundary of the observations there is a possibility of edge effects in the map. It is also possible that the flow is not in near-geostrophic balance in this small region. In either case, this is the only region where the observed and geostrophic velocities and vorticities are very different. In general, the observed flow is nearly

geostrophic and relatively small adjustments are required to achieve the geostrophic constraint.

The evolution of the front over the observed time period may be examined as a function of across-front distance and time through Hovmöller plots (Fig. 6). The front appears in the region during the second week of April and intensifies over the next weeks. The front is strongest as measured by the horizontal gradients of potential density and salinity, and by the strength of the alongfront geostrophic velocity near 21 April. A second period of frontal intensification takes place around 5 May. A relatively continuous filament of alongfront flow is seen on the right side of the observed region. The important result to be taken from the Hovmöller plots is that the front that appeared in the first half of April persisted through the rest of the observed period, providing a site for possible downward flow.

A central objective is to quantify the three-dimensional circulation including vertical velocity. For a first look at vertical velocity derived from the QG omega equation in Eq. (17), consider a sequence of maps at 50-m depth (Fig. 7) spanning the period during April when the front was strong. The front in potential density first appears at the north side of the observed region (Fig. 7a), with weak downwelling in the
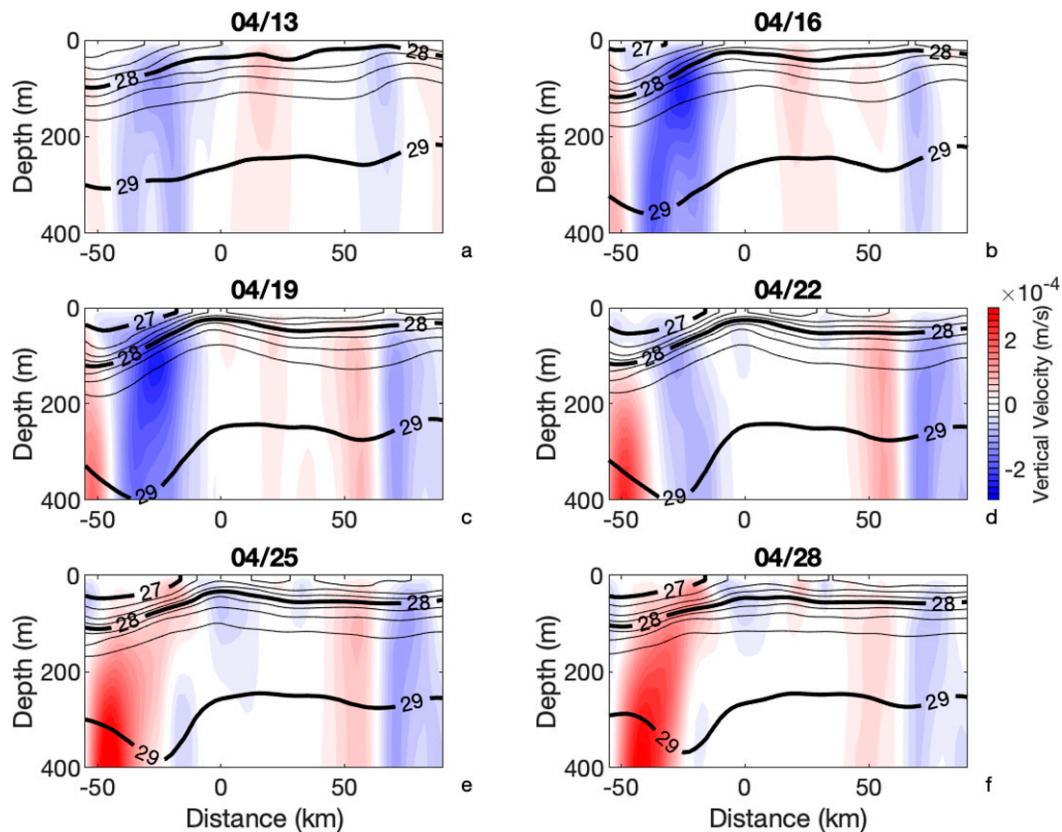
FIG. 8. Vertical velocity on the central lane at 3-day intervals in the time period 13–28 Apr as a function of across-front distance and depth. Vertical velocity is shown with color shading and potential density is contoured with an interval of 0.25 kg m^{-3}. Downward vertical velocity is strongest on the central lane on 19 Apr.

vicinity. The front intensifies over the next three days (Fig. 7b), along with a stronger alongfront jet and greater downwelling. This frontogenetic feature propagates southward over the next several days (Figs. 7c,d). The feature begins to exit the region on 25 April, with remnants still visible on 28 April (Figs. 7e,f). A region of upwelling propagates southward following the downwelling feature. This upward flow appears weaker than the downward flow and is accompanied by less intense horizontal gradients of density (Figs. 7e,f) consistent with upwelling being associated with frontolysis. To summarize, the co-occurrence of the strong front and downwelling in a propagating coherent feature is worthy of note.

The vertical structure of the vertical velocity may be examined using sections along the central lane (Fig. 8). When the front first appears prominently in the north on 13 April there is already weak downwelling on the central lane (Fig. 8a). This downwelling increases in intensity through 19 April (Figs. 8b,c) and then weakens over the next several days (Figs. 8d–f). This behavior is consistent with the southward propagation apparent in the maps (Fig. 7). In general, the strongest downward flow occurs near 100-m depth just under where density gradients are highest. A region of upwelling occurs on the less dense side of the front and gradually

strengthens as the downwelling cell propagates southward (Figs. 8d–f). The combination of downward flow on the dense side of the front and upward flow on the light side tends to cause the front to flatten, consistent with a baroclinic instability. The strongest upward flows are relatively deeper than the peak downward flows. In summary, downwelling is strongest beneath where stratification is maximum, and the sense of the overturning circulation is to flatten the front.

The ageostrophic horizontal velocity indicates the direction of the overturning circulation. Consider the maps of vertical velocity during the period of frontal intensification, with the horizontal ageostrophic velocity superimposed (Fig. 9). At a depth of 50 m, above the maximum in vertical velocity, the downwelling regions are generally fed by ageostrophic flow from the light side of the front. The horizontal ageostrophic flow must be convergent at this depth of the downwelling regions by the continuity equation [Eq. (12)], and the ageostrophic flow goes from the regions of upwelling to those of downwelling. This convergence is mostly achieved by having weaker ageostrophic flow on the dense side of the front, and across-front flow on the light side. The direction of the overturning cell is thus to cause the front to flatten, again consistent with a baroclinic instability.
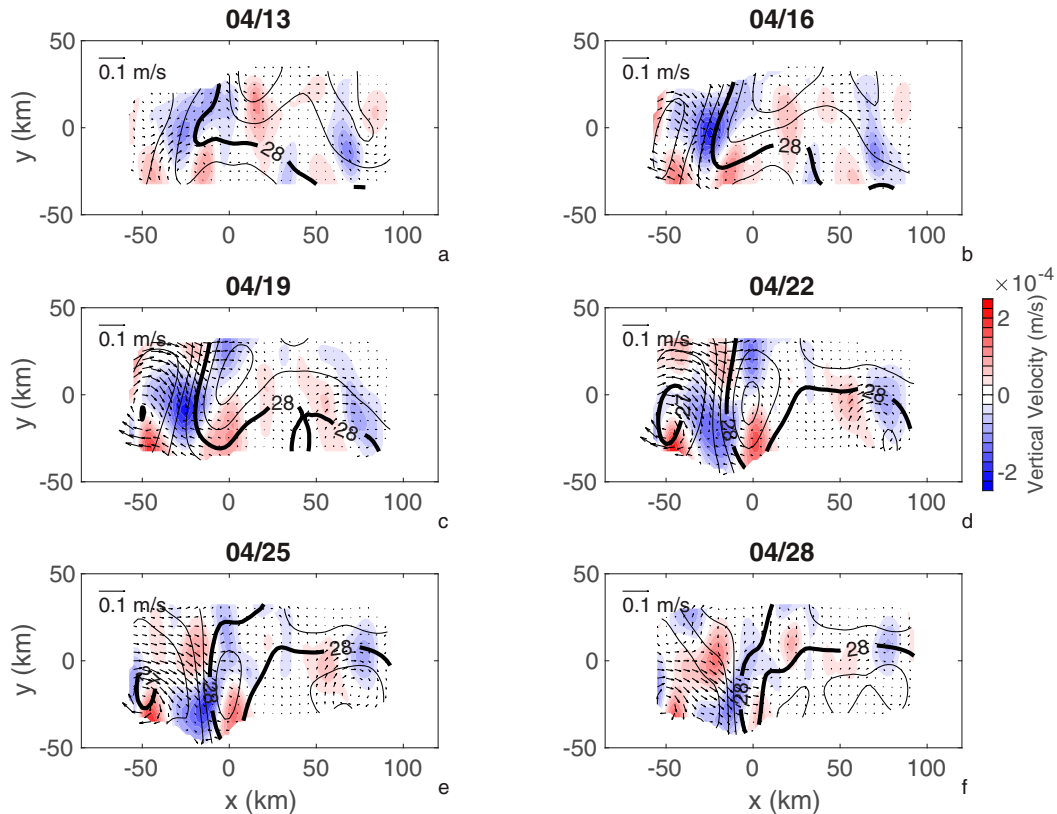
FIG. 9. Vertical velocity at 50 m as in Fig. 7, but with ageostrophic velocity plotted as vectors. Note the scale in the upper-left corner of each panel. The downward flow is accompanied by horizontally convergent ageostrophic velocity.

An examination of tracers on an isopycnal surface helps to diagnose the three-dimensional pathways as a function of time. Here we examine three days (Figs. 10–12) during the period of frontal intensification on an isopycnal (28.1 kg m^{-3}) that initially outcrops to the north. An animation spanning the entire glider deployment (see the online supplemental material: https://doi.org/10.1175/JPO-D-21-0181.s1). allows a more detailed examination. On 13 April (Fig. 10) the isopycnal outcrops in the north, sloping especially strongly on the west side of the outcrop where there is a high of chlorophyll fluorescence (Fig. 10a) likely driven by the uplift of this isopycnal into the euphotic zone. This high chlorophyll fluorescence provides a valuable tracer. A region of downwelling occurs to the west of the outcrop consistent with the geostrophic current heading in the direction of the deepening isopycnal. The tracers salinity, acoustic backscatter, and potential vorticity are unremarkable near the outcrop at this time. The outcrop appears related to the cape near 36.8°N, 2.1°W (Fig. 1), which barely touches the region in the map near x = 30 km, y = 50 km (Fig. 10). This initial appearance of the front thus seems caused by coastal processes affected by topography (Capó et al. 2021). A high in chlorophyll fluorescence also appears in the eastern part of the observed region. This high is related to a relatively weak outcrop that occurred a few days earlier. An area of low potential vorticity accompanies the high in chlorophyll

fluorescence. This co-occurrence of tracer extrema may be a result of the alignment of tracer gradients by stirring (Ferrari and Paparella 2003; Hodges and Rudnick 2006).

On 19 April the 28.1 kg m^{-3} isopycnal is strongly sloping downward toward the west, less dense side of the front (Fig. 11). The outcrop has disappeared and a streamer high in chlorophyll fluorescence and acoustic backscatter extends along the dense side of the front (Figs. 11a,c). The high in these tracers extends down to roughly 50-m depth. Along this streamer there is also evidence of high salinity indicative of Mediterranean water from the dense side of the front (Fig. 11b). Potential vorticity calculated from either geostrophic or observed velocity shows a high on the cyclonic side of the front (Figs. 11d,f). This high is due both to increased stratification and strong positive relative vorticity in this region. The frontal jet is well established and directed slightly toward the less dense side of the front, causing downwelling at the nose of the streamer (Fig. 11e). Peak downward velocities approach 2.8 × 10^{-4} m s^{-1} (24 m day^{-1}). The co-occurrence of streamers of every observed tracer on a plunging isopycnal consistent with the inference of vertical velocity by the omega equation is evidence of the three-dimensional pathway that is the focus of this work.

By 25 April, the region of strong downwelling has propagated southward to the edge of the observed region (Fig. 12).
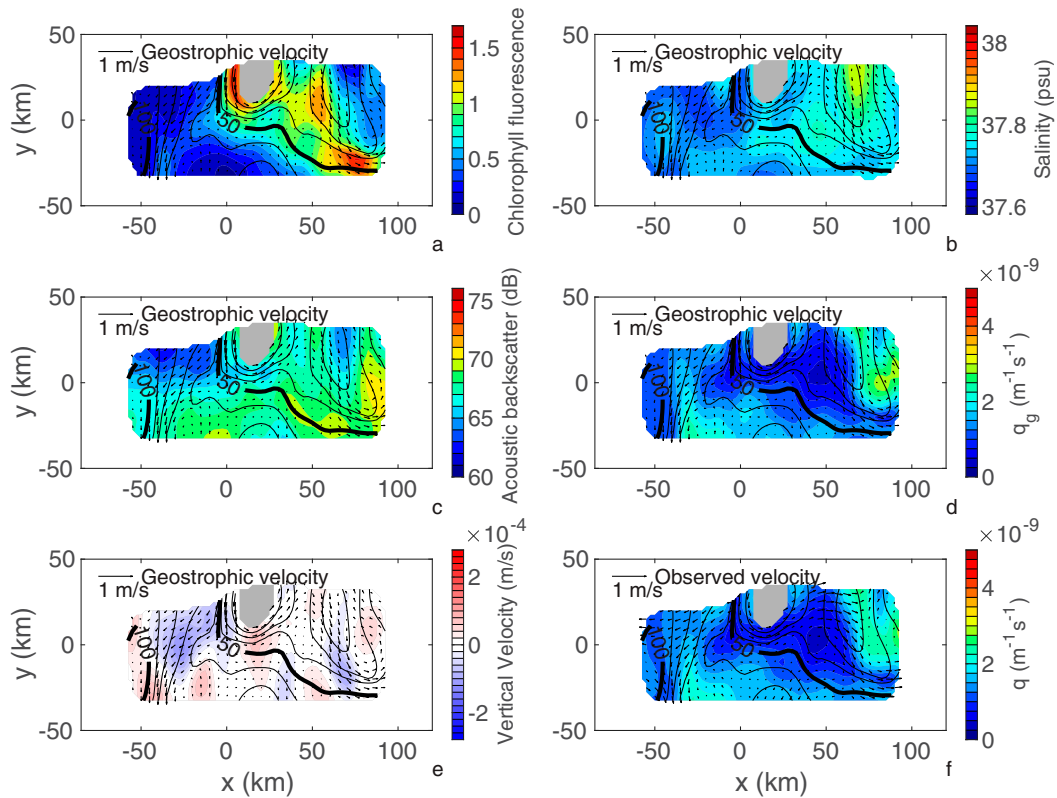
FIG. 10. Maps on the 28.1 kg m^{-3} isopycnal on 13 Apr of (a) chlorophyll fluorescence, (b) salinity, (c) acoustic backscatter, (d) geostrophic potential vorticity, (e) vertical velocity, and (f) potential vorticity. Variables are shown with color shading, and depth contours are in black. Geostrophic velocity in (a)–(e) and observed velocity in (f) is shown using vectors, with a scale in the upper-left corner of each panel. The gray shading indicates the mapped region where the isopycnal does not exist because it is outcropped.

An elongated region on the dense side of the front has highs in all the tracers. As the sharpest part of the front leaves the region a broader portion of the front follows with weak upwelling. The several-day event described here was the strongest observed during the 2-month occupation of the area. Another period of frontal strengthening followed in early May (see the online supplemental material), and the front remained until the gliders were gathered for recovery.

An examination of the density conservation equation [Eq. (13)] addresses the relative importance of horizontal and vertical advection and the resulting time rate of change of density. Terms in Eq. (13) are shown in Fig. 13 with the sign convention on advection as if the terms were on the right-hand side of the equation balancing the rate of change term. In calculating advection, vertical velocity is from the omega equation [Eq. (17)] and the geostrophic velocity is used for horizontal advection. The time rate of change of density is calculated as the sum of the advection terms. If the balance were steady then the advection terms would be equal in magnitude and opposite in sign (Figs. 13b,c). There is some tendency for this steady balance in the region of strongest downwelling, with the decrease in density caused by downward flow somewhat balanced by the increase in density caused by flow from

the dense side of the front. However, the balance is not exact and the time rate of change of density has a magnitude comparable to that of advection and adopts both signs. The examination of the density conservation equation suggests that all the terms in Eq. (13) are important.

The tendency for the vertical velocity to flatten the front can be quantified by calculating the covariance of vertical velocity and density. The covariance $\langle w'\rho' \rangle$ is calculated as a function of time and depth with the angle brackets denoting a horizontal average over the area of the map, and the primes indicating fluctuations relative to the horizontal average. The result is presented in units of heat flux using a constant value 1.7325×10^7 J kg^{-1} for the ratio of the specific heat to the thermal expansion coefficient. The equivalent heat flux tends to be positive, consistent with light warm water rising and dense cold water sinking (Fig. 14). The maximum heat flux is near 100-m depth (Fig. 14), just beneath the region of highest stratification. The peak values of heat flux approach 80 W m^{-2} during the downwelling event in mid- to late April. A second period of high heat flux of over 60 W m^{-2} occurs in early May. The pattern of heat flux with a maximum near 100 m serves to warm the ocean above and cool below, resulting in a tendency to stratify consistent with a baroclinic instability in the QG approximation. The brief
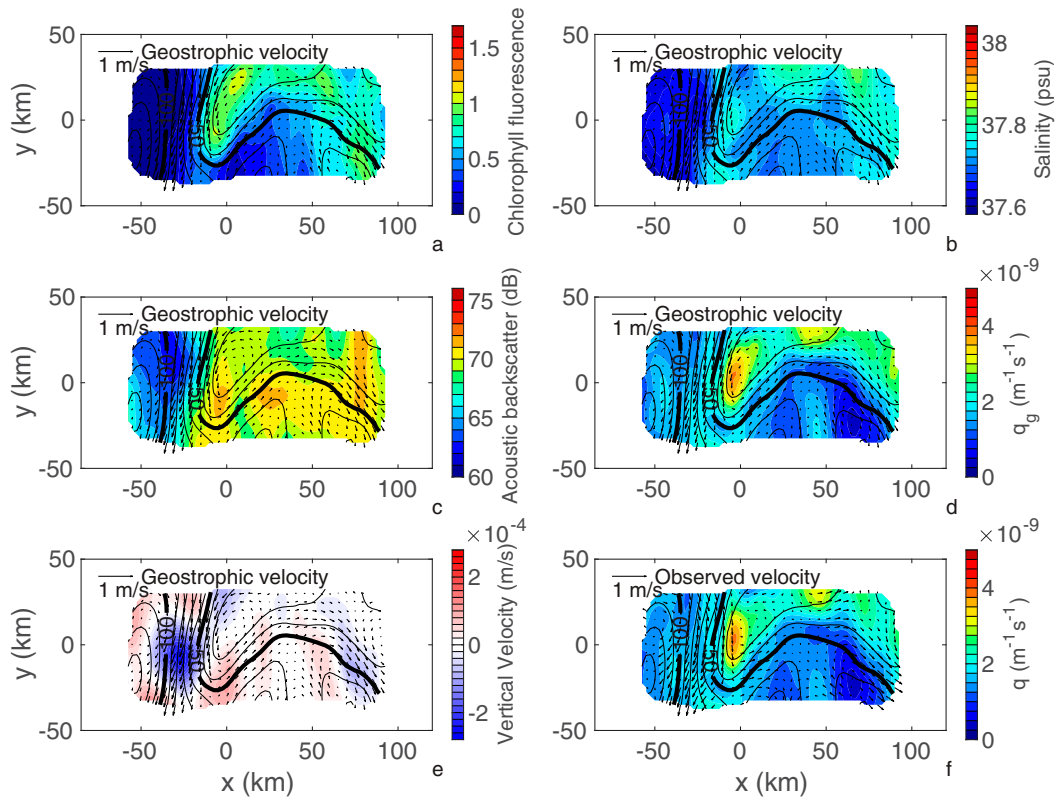
FIG. 11. As in Fig. 10, but on 19 Apr.

period of negative heat flux in early April appears related to the initial formation of the front on the north side of the observed region. In summary, the heat flux supports the notion of the tendency for a front to flatten in these QG dynamics.

The QG approximation used in this study is admittedly simple, but it is complete in the sense that the continuity, density, and momentum equations are all exactly satisfied. There are many other ways to infer the vertical velocity given four-dimensional measurements of velocity and density fields, distinguished by the dynamics used. Here we examine a few of the possibilities for the calculation of vertical velocity. The rate of change of density can be calculated directly from the maps of density, as opposed to inferred using QG dynamics (as in Fig. 13a). Using this directly calculated rate of change of density, vertical velocity can then be inferred using geostrophic horizontal velocity in Eq. (13), as shown in Fig. 15b. Relative to the vertical velocity from the omega equation (Fig. 15a), the vertical velocity from density conservation and geostrophic advection is larger, although much of the pattern of downward velocity remains. The similarities between these two estimates of vertical velocity supports the use of the QG approximation. Differences between these estimates may be due to the limitations of quasigeostrophy or the influence on the observations of poorly resolved higher-frequency motions like those caused by internal waves. To consider a more expansive set of dynamics, we calculate the vertical velocity using the observed horizontal velocity (Fig. 15c) in the density

Eq. (13). The resulting vertical velocity is larger still, at roughly twice the magnitude of the QG vertical velocity. A downwelling region exists (Fig. 15c) near where there are similar downwelling areas using geostrophic advection (Figs. 15a,b), while a strong upwelling region appears in the north. Finally, a calculation of vertical velocity (Fig. 15d) is done by integrating the continuity Eq. (12) downward from zero at the surface, but with observed horizontal velocity. In one sense this is the simplest set of dynamics in that volume conservation is an obvious requirement for an incompressible fluid. On the other hand, this allows the largest range of possibilities for the other conservation equations. The vertical velocity in Fig. 15d has large swings between values approaching about 100 m day^{-1}, roughly 4 times the size of the maximum from the QG omega equation. For the estimates of vertical velocity using observed horizontal velocity, rather than those using velocity constrained to be in geostrophic balance, we must acknowledge the possibility that inadequately resolved internal waves may affect the result. The differences between the vertical velocity calculated using only density conservation and only volume conservation (Figs. 15c,d) indicate that both equations cannot be simultaneously satisfied by either vertical velocity given the observed velocity and density fields. In particular, it is hard to imagine how density stratification could be maintained in the presence of vertical velocity of 100 m day^{-1}. Ultimately, the value of the QG omega equation is that the resulting vertical velocity does satisfy a complete set of dynamics.
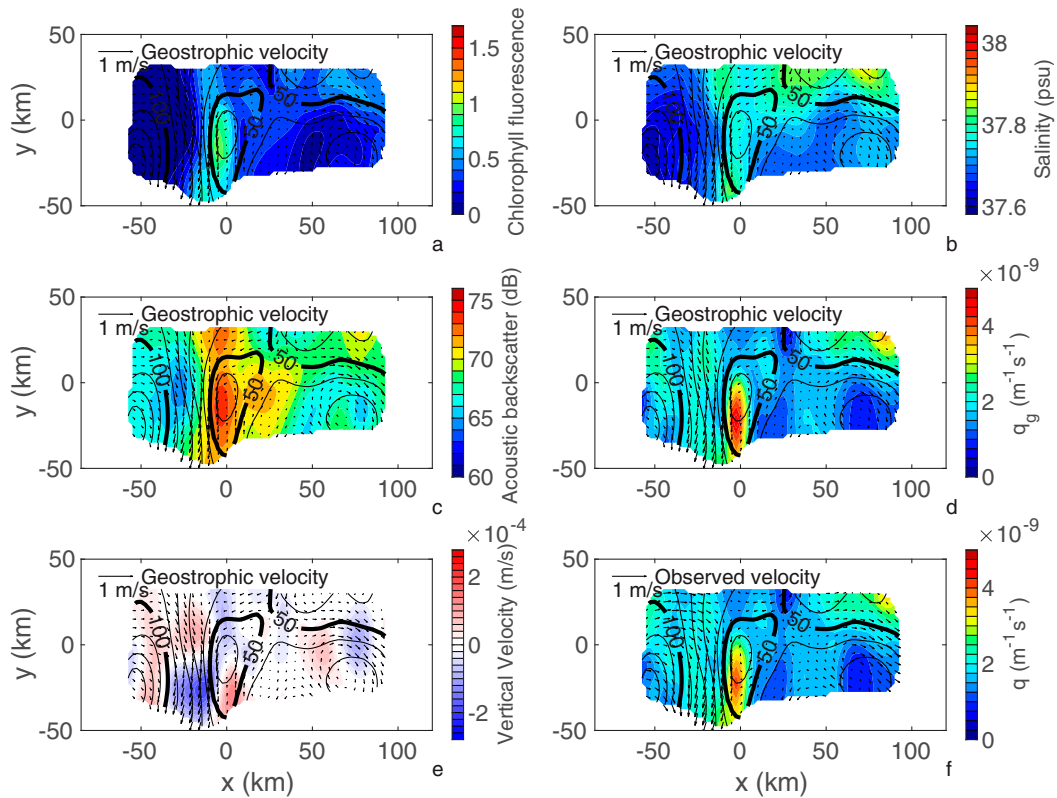
FIG. 12. As in Fig. 10, but on 25 Apr.

A direct measure of vertical velocity was made by programming a glider to follow a chosen isotherm. To follow an isotherm, the glider actively monitored temperature and pressure and adjusted buoyancy to make fast cycles about the chosen temperature while drifting horizontally. During these drifts, the glider's ballast was adjusted to have zero pitch and zero roll and was not further controlled. Seven 24-h drifts were done, and one example is shown in Fig. 16. The location for each drift was chosen on the basis of the most recently completed section in an attempt to tag regions where downwelling was likely. The chosen temperature in this case was 14°C, and it took the glider about 2.5 h to locate the isotherm. From that point on, the glider controlled its depth to stay within a standard deviation of 0.2°C of the isotherm while oscillating with a period of 12 min. During this time the standard deviation of pressure was 4 dbar. The mean potential density over the drift was 28.7 kg m^{-3} with a standard deviation of 0.1 kg m^{-3} so it is reasonable to conclude that the glider followed an isopycnal. During a period from roughly hour 8 to hour 15 there was a downward displacement of 15 m, equivalent to a vertical velocity of about 50 m day^{-1}. Averaged over the complete day of the drift, the observed downward velocity was thus 15 m day^{-1}, consistent with inferences of vertical velocity from the omega equation. This drift had the largest vertical velocity observed by the isotherm-following glider. Given the spatial and temporal intermittency of vertical velocity, and the challenge of putting the glider in

best position to observe downward flow, perhaps it is not surprising that only one drift had large downwelling.

5. Discussion

This work addressed the four-dimensional pathways of subduction at the AO Front. A fleet of seven gliders produced tracer fields in the vicinity of the front over a 2-month period. Tracers included potential density, salinity, the dynamical tracer potential vorticity, and the biological tracers chlorophyll fluorescence and acoustic backscatter. The horizontal velocity field was observed by the glider fleet and a geostrophic velocity inferred using a variational method. The vertical velocity and horizontal ageostrophic velocity were derived from the QG omega equation. A downwelling event was observed as supported by the four-dimensional evolution of tracers and velocity. The vertical density flux produced by downwelling dense water and upwelling light water tended to cause a slumping and restratification of the front. Put together, the tracers and velocity fields supported the notion of a pathway of water from the surface to the interior ocean.

This study using a fleet of underwater gliders is part of a continuing progression of improving approaches to ocean surveys. The pioneering work on ocean fronts was accomplished by doing CTD stations spanning frontal regions (e.g., Roden 1975). Starting in the 1980s an explosion of activity centered around ocean fronts was ushered in by the arrival of rapidly
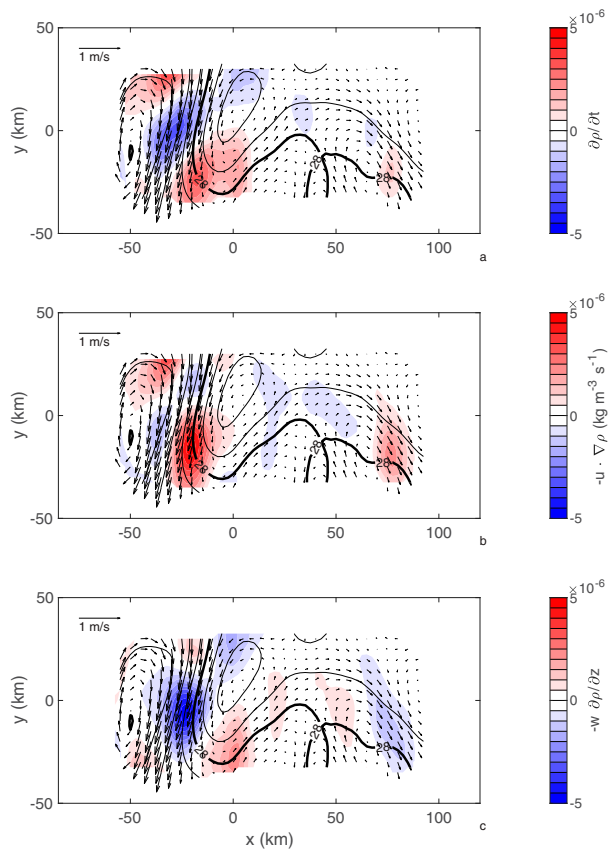
FIG. 13. Terms in the density conservation equation at 50 m on 19 Apr. Shown are (a) time rate of change of density, (b) horizontal advection of density, and (c) vertical advection of density. The signs of the advection terms are the opposite of how they appear in Eq. (13) so that their sum is equal to the time rate of change of density. Potential density is contoured in black, with an interval of 0.25 kg m^{-3}.
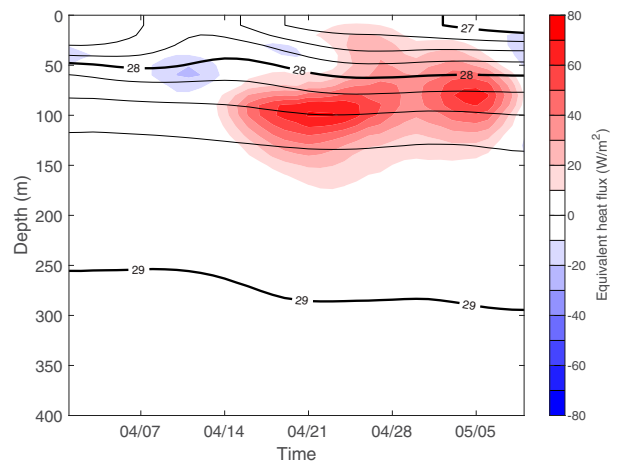

FIG. 14. Equivalent heat flux caused by the covariance of vertical velocity and density. The covariance is averaged over the area of the survey, and the expansion coefficient and specific heat are taken to be constant. The mean potential density averaged over the area of the surveyed is contoured in black, with an interval of 0.25 kg m^{-3}. Note the maxima near 100-m depth, implying a convergence of the vertical heat flux above and a divergence below and thus a tendency to stratify.

towed vehicles (e.g., SeaSoar; Pollard 1986). While there have been some advances made in rapid profiling using lighter equipment (e.g., Underway CTD; Rudnick and Klinke 2007), the fundamental limitations on research vessel speed and cruise duration remain. The basic challenge in observing a front was first to find the front, and second to be at the front at the time when the largest ageostrophic flows were occurring. Rather than focus on the strongest events, a strand of research attempted to generate statistics of horizontal gradients using long linear surveys (Rudnick and Ferrari 1999; Cole et al. 2010). The advent of underwater gliders (Rudnick et al. 2004) offered new opportunities to observe frontal processes, although the slowness of gliders put a limit on the horizontal wavelengths observable by a single glider (Rudnick and Cole 2011). The coordinated fleet of gliders used in this study has a total profiling speed of the sum of the speeds of the individual gliders, approaching the speed of a ship survey. The real value of the glider fleet is its persistence, as it can be at a frontal site long enough to wait for the largest ageostrophic events.

Five tracers, physical and biological, are used here to identify subduction pathways. The value of tracers in studying ocean circulation is to identify extrema and then to track them as they are advected. Absent strong localized sources and sinks the extrema indicate pathways even in the presence of mixing that may erode the extrema. Potential density is particularly useful as a tracer because its distribution is monotonic in depth. The objective is then to identify tracers with extrema on surfaces of constant potential density. In this study, we examine salinity, potential vorticity, chlorophyll fluorescence and acoustic backscatter on a potential density surface that outcrops. Each tracer has value as a maximum because of its origin. Salinity and potential vorticity have maxima on the dense, cyclonic side of the front where water subducts. The biological tracers chlorophyll fluorescence and acoustic backscatter are maxima near the surface, so they are useful to indicate downwelling. Finding a maximum in a biological tracer at depth suggests that there was downward flow during the tracer's history even if there is not vertical velocity at the time the maximum is observed. The initial distribution of a tracer is an important consideration, as a tracer with no extremum has little value. Having several tracers is an essential aspect of this work.

The inference of vertical velocity depends on the assumed dynamics. In this study, we use a QG omega equation to infer vertical velocity from a sequence of maps. The QG omega equation has long been used for diagnosis from ocean surveys. Work over the years has included additions of mixing (Nagai et al. 2006), extension to the semigeostrophic approximation (Pinot et al. 1996), a generalized omega equation (Viúdez et al. 1996b; Pallàs-Sanz et al. 2010), an inverse approach (Thomas et al. 2010), and examinations of errors in realizable
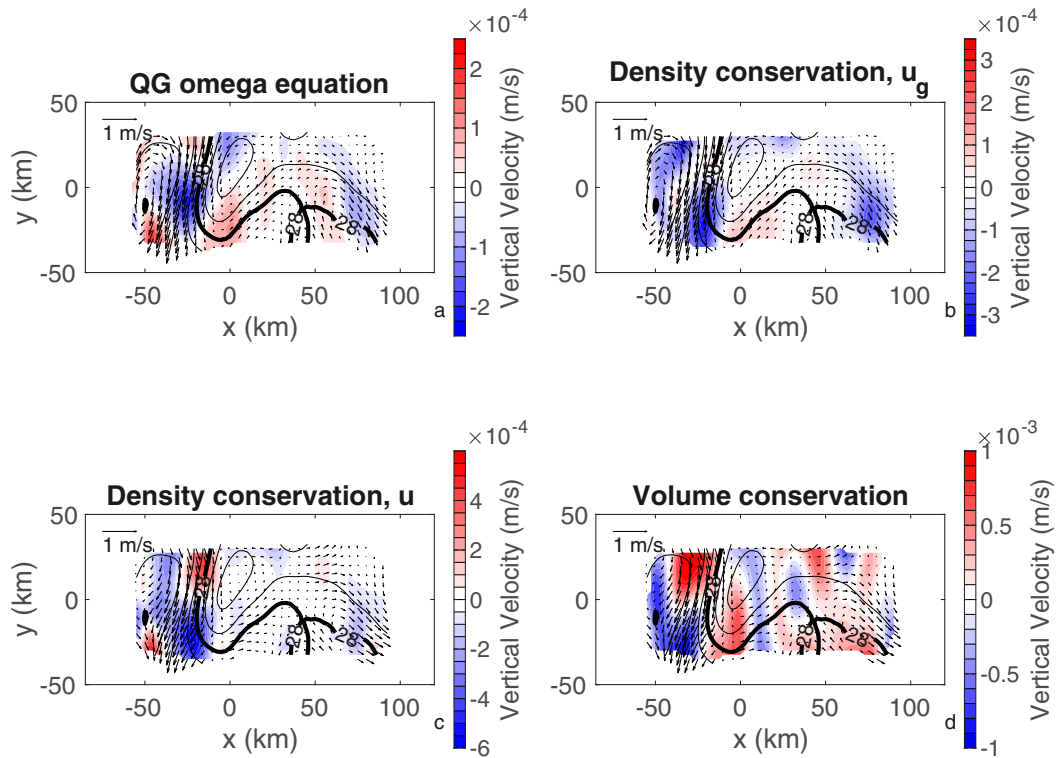
FIG. 15. Vertical velocity at 50 m on 19 Apr, calculated assuming different dynamics: (a) the quasigeostrophic omega equation, (b) density conservation with advection by the geostrophic velocity, (c) density conservation with advection by the observed horizontal velocity, and (d) volume conservation using the observed horizontal velocity. Isopycnals are indicated by black contours. Horizontal velocity is shown using vectors, with geostrophic velocity in (a) and (b) and observed velocity in (c) and (d). Note the different scales for vertical velocity in each panel.

surveys and alternate sampling strategies (Allen et al. 2001b; Rixen et al. 2001). In this study we have opted for a relatively simple form of the QG omega equation with the main advance being the temporal sequence of vertical velocity fields. The QG approximation is used because of its simplicity,

FIG. 16. Isotherm tracking for 24 h during 30 Apr–1 May. Shown are time series of (a) temperature and potential density and (b) pressure.

even though the ratio of relative to planetary vorticity approaches unity occasionally (Fig. 5). An advantage of this approach is that vertical velocity satisfies a complete set of dynamical equations conserving volume, density, and momentum. Vertical velocity may also be inferred using any one of the full set of equations, with the disadvantage that the inferred velocity may not satisfy the other equations in the complete dynamics. We consider dynamics including density conservation with geostrophic advection, density conservation with observed advection, and the continuity equation (Figs. 15b–d). While these approaches may seem simpler than using the QG omega equation, they all result in higher vertical velocities. The solution of the continuity equation, in particular, has unreasonably large vertical velocities that would not allow density conservation, and is likely contaminated by unresolved internal waves. Constraining horizontal velocity to be geostrophic and the QG omega equations is preferred here for the estimation of vertical velocity.

The solution of the QG omega equation may be considered a simple form of data assimilation. The resulting ageostrophic velocity field satisfies a complete set of dynamics and is faithful to the data. The state of the art in regional data assimilation (Edwards et al. 2015) involves models with primitive equations that allow many more processes than would be expressed in a QG approximation. The realism of the
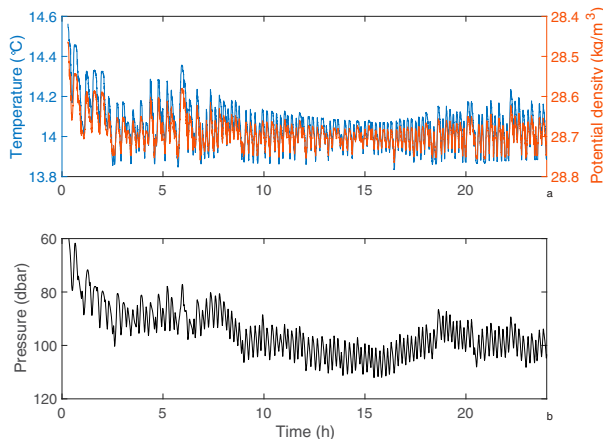
processes in an advanced data assimilative model may have a cost that solutions are not as close to the data as those in this paper. The observation-centric approach here may have value as a reference against which the more complex data assimilations may be compared. For example, the Western Mediterranean Operational model (WMOP; Juza et al. 2016) found vertical velocities of tens of meters per day at the AO Front (Garcia-Jove et al. 2022). Models with coupled biological dynamics have shown how the physical processes at fronts in the Alboran Sea modulate primary production (Oguz et al. 2016, 2017). The way forward for oceanography is surely toward combined observing and modeling systems.

The direct measurement of vertical velocity is a longstanding challenge in oceanography often met using actively controlled neutrally buoyant Lagrangian floats (D'Asaro 2003). Adding this capability to an underwater glider, as done in this study, is a natural extension to what is essentially a buoyancy-controlled profiling float with wings. The glider was controlled to cycle rapidly around a chosen isotherm, similar to control algorithms used on some floats (D'Asaro 2018). Given that the vertical velocity is intermittent in space and time, a challenge was to position the glider in the place where signals would be largest. Of seven 1-day drifts, we observed one example of a vertical velocity as large as 50 m day^{-1} over several hours and 15 m day^{-1} over the full day's drift. For comparison, Johnson et al. (2020) used a neutrally buoyant float to observe vertical velocities as large as 60–120 m day^{-1} over time scales of hours, with a net downward displacement of about 10 m over a day. Overall, the Lagrangian approach to observing vertical velocity has proven valuable even with the challenges of intermittency.

There is a net density flux associated with a slumping front as water on the dense side tends to descend and water on the light side tends to ascend. This density flux is to be expected for a baroclinic instability (Haine and Marshall 1998). We report the density flux in units of an equivalent heat flux by multiplying by a constant ratio of the specific heat to the thermal expansion coefficient. The maximum value approaches 80 W m^{-2} near 100-m depth. For comparison, the annual mean surface heat flux over the Alboran Sea is about 40 W m^{-2} with the ocean receiving heat from the atmosphere (Song and Yu 2017). A similar omega equation calculation using data from the Azores front yielded a maximum heat flux of about 15 W m^{-2} (Rudnick 1996), consistent with the difference in horizontal gradients of density in the Azores and AO Fronts. While much larger heat fluxes of 2000 W m^{-2} have been reported over time scales of hours (Johnson et al. 2020), the estimate in this paper is representative of time scales of days. In summary, the vertical flux during the restratification of a front is a useful measure of the strength of the ageostrophic circulation.

6. Conclusions

The four-dimensional dataset collected by our fleet of underwater gliders allowed a time-dependent description of the pathways of water downward from the surface in the vicinity of a strong front. A suite of five physical and biological tracers and inferences based on QG dynamics contributed to the illumination of these pathways. To our knowledge, the observational resolution in time and space achieved here by several autonomous platforms is unprecedented, especially with respect to its temporal persistence. Continuing work on this dataset involves an examination of higher-order dynamics, including the semigeostrophic approximation. In general, the use of autonomous platforms for sustained surveying of mesoscale and smaller features is a research activity of growing importance to which we think this work is a fundamental contribution.

Data availability statement. Spray underwater glider data are available online (https://spraydata.ucsd.edu; Rudnick 2021). SOCIB Slocum glider data are also available online (https://www.socib.eu; Zarokanellos et al. 2021).

REFERENCES

Allen, J. T., and D. A. Smeed, 1996: Potential vorticity and vertical velocity at the Iceland-Faeroes Front. *J. Phys. Oceanogr.*, **26**, 2611–2634, https://doi.org/10.1175/1520-0485(1996)026<2611:PVAVVA>2.0.CO;2.

——, ——, J. Tintoré, and S. Ruiz, 2001a: Mesoscale subduction at the Almeria–Oran front: Part 1: Ageostrophic flow. *J. Mar. Syst.*, **30**, 263–285, https://doi.org/10.1016/S0924-7963(01)00062-8.

——, ——, A. J. G. Nurser, J. W. Zhang, and M. Rixen, 2001b: Diagnosis of vertical velocities with the QG omega equation: An examination of the errors due to sampling strategy. *Deep-Sea Res. I*, **48**, 315–346, https://doi.org/10.1016/S0967-0637(00)00035-2.

Arnone, R. A., D. A. Wiesenburg, and K. D. Saunders, 1990: The origin and characteristics of the Algerian Current. *J. Geophys. Res.*, **95**, 1587–1598, https://doi.org/10.1029/JC095iC02p01587.

Bergeron, T., 1937: On the physics of fronts. *Bull. Amer. Meteor. Soc.*, **18**, 265b–275, https://doi.org/10.1175/1520-0477-18.9.265b.

Bretherton, F. P., R. E. Davis, and C. B. Fandry, 1976: A technique for objective analysis and design of oceanographic

experiments applied to MODE-73. *Deep-Sea Res.*, **23**, 559–582, https://doi.org/10.1016/0011-7471(76)90001-2.

Capó, E., J. C. McWilliams, E. Mason, and A. Orfila, 2021: Intermittent frontogenesis in the Alboran Sea. *J. Phys. Oceanogr.*, **51**, 1417–1439, https://doi.org/10.1175/JPO-D-20-0277.1.

Cole, S. T., D. L. Rudnick, and J. A. Colosi, 2010: Seasonal evolution of upper-ocean horizontal structure and the remnant mixed layer. *J. Geophys. Res.*, **115**, C04012, https://doi.org/10.1029/2009JC005654.

Courant, R., and D. Hilbert, 1953: *Methods of Mathematical Physics.* Vol. I. Interscience Publishers, 561 pp.

D'Asaro, E. A., 2018: Oceanographic floats: Principles of operation. *Observing the Oceans in Real Time*, R. Venkatesan et al., Eds., Springer, 77–98, https://doi.org/10.1007/978-3-319-66493-4_5.

——, 2003: Performance of autonomous Lagrangian floats. *J. Atmos. Oceanic Technol.*, **20**, 896–911, https://doi.org/10.1175/1520-0426(2003)020<0896:POALF>2.0.CO;2.

Edwards, C. A., A. M. Moore, I. Hoteit, and B. D. Cornuelle, 2015: Regional ocean data assimilation. *Annu. Rev. Mar. Sci.*, **7**, 21–42, https://doi.org/10.1146/annurev-marine-010814-015821.

Ferrari, R., and F. Paparella, 2003: Compensation and alignment of thermohaline gradients in the ocean mixed layer. *J. Phys. Oceanogr.*, **33**, 2214–2223, https://doi.org/10.1175/1520-0485(2003)033<2214:CAAOTG>2.0.CO;2.

Garcia-Jove, M., B. Mourre, N. D. Zarokanellos, P. F. J. Lermusiaux, D. L. Rudnick, and J. Tintoré, 2022: Frontal dynamics in the Alboran Sea—Part II: Processes for vertical velocities development. *J. Geophys. Res. Oceans*, https://doi.org/10.1029/2021JC017428, in press.

Haine, T. W., and J. Marshall, 1998: Gravitational, symmetric, and baroclinic instability of the ocean mixed layer. *J. Phys. Oceanogr.*, **28**, 634–658, https://doi.org/10.1175/1520-0485(1998)028<0634:GSABIO>2.0.CO;2.

Hodges, B. A., and D. L. Rudnick, 2006: Horizontal variability in chlorophyll fluorescence and potential temperature. *Deep-Sea Res. I*, **53**, 1460–1482, https://doi.org/10.1016/j.dsr.2006.06.006.

Hoskins, B. J., I. Draghici, and H. C. Davies, 1978: A new look at the ω-equation. *Quart. J. Roy. Meteor. Soc.*, **104**, 31–38, https://doi.org/10.1002/qj.49710443903.

Johnson, L., C. M. Lee, E. D'Asaro, L. Thomas, and A. Shcherbina, 2020: Restratification at a California Current upwelling front. Part I: Observations. *J. Phys. Oceanogr.*, **50**, 1455–1472, https://doi.org/10.1175/JPO-D-19-0203.1.

Juza, M., and Coauthors, 2016: SOCIB operational ocean forecasting system and multi-platform validation in the Western Mediterranean Sea. *J. Oper. Oceanogr.*, **9**, S155–S166, https://doi.org/10.1080/1755876X.2015.1117764.

Macías, D., M. Bruno, F. Echevarria, A. Vazquez, and C. M. Garcia, 2008: Meteorologically-induced mesoscale variability of the North-western Alboran Sea (southern Spain) and related biological patterns. *Estuarine Coastal Shelf Sci.*, **78**, 250–266, https://doi.org/10.1016/j.ecss.2007.12.008.

Macias, D., E. Garcia-Gorriz, and A. Stips, 2016: The seasonal cycle of the Atlantic Jet dynamics in the Alboran Sea: Direct atmospheric forcing versus Mediterranean thermohaline circulation. *Ocean Dyn.*, **66**, 137–151, https://doi.org/10.1007/s10236-015-0914-y.

Mahadevan, A., 2016: The impact of submesoscale physics on primary productivity of plankton. *Annu. Rev. Mar. Sci.*, **8**, 161–184, https://doi.org/10.1146/annurev-marine-010814-015912.

——, A. Pascual, D. L. Rudnick, S. Ruiz, J. Tintoré, and E. D'Asaro, 2020: Coherent pathways for vertical transport from the surface

ocean to interior. *Bull. Amer. Meteor. Soc.*, **101**, E1996–E2004, https://doi.org/10.1175/BAMS-D-19-0305.1.

McWilliams, J. C., 2016: Submesoscale currents in the ocean. *Proc. Roy. Soc.*, **472A**, 20160117, https://doi.org/10.1098/rspa.2016.0117.

Nagai, T., A. Tandon, and D. L. Rudnick, 2006: Two-dimensional ageostrophic secondary circulation at ocean fronts due to vertical mixing and large-scale deformation. *J. Geophys. Res.*, **111**, C09038, https://doi.org/10.1029/2005JC002964.

Niller, P. P., and R. W. Reynolds, 1984: The three-dimensional circulation near the eastern North Pacific subtropical front. *J. Phys. Oceanogr.*, **14**, 217–230, https://doi.org/10.1175/1520-0485(1984)014<0217:TTDCNT>2.0.CO;2.

Oguz, T., B. Mourre, and J. Tintoré, 2016: Upstream control of the frontal jet regulating plankton production in the Alboran Sea (Western Mediterranean). *J. Geophys. Res. Oceans*, **121**, 7159–7175, https://doi.org/10.1002/2016JC011667.

——, ——, and ——, 2017: Modulation of frontogenetic plankton production along a meandering jet by zonal wind forcing: An application to the Alboran Sea. *J. Geophys. Res. Oceans*, **122**, 6594–6610, https://doi.org/10.1002/2017JC012866.

Pallàs-Sanz, E., T. M. S. Johnston, and D. L. Rudnick, 2010: Frontal dynamics in a California Current system shallow front: 2. Mesoscale vertical velocity. *J. Geophys. Res.*, **115**, C12068, https://doi.org/10.1029/2010JC006474.

Pietri, A., X. Capet, F. D'Ovidio, M. Levy, J. Le Sommer, J. M. Molines, and H. Giordani, 2021: Skills and limitations of the adiabatic omega equation: How effective is it to retrieve oceanic vertical circulation at mesoscale and submesoscale? *J. Phys. Oceanogr.*, **51**, 931–954, https://doi.org/10.1175/JPO-D-20-0052.1.

Pinot, J. M., J. Tintoré, and D. P. Wang, 1996: A study of the omega equation for diagnosing vertical motions at ocean fronts. *J. Mar. Res.*, **54**, 239–259, https://doi.org/10.1357/0022240963213358.

Pollard, R., 1986: Frontal surveys with a towed profiling conductivity/temperature/depth measurement package (SeaSoar). *Nature*, **323**, 433–435, https://doi.org/10.1038/323433a0.

Pollard, R. T., and L. A. Regier, 1992: Vorticity and vertical circulation at an ocean front. *J. Phys. Oceanogr.*, **22**, 609–625, https://doi.org/10.1175/1520-0485(1992)022<0609:VAVCAA>2.0.CO;2.

Renault, L., T. Oguz, A. Pascual, G. Vizoso, and J. Tintoré, 2012: Surface circulation in the Alboran Sea (western Mediterranean) inferred from remotely sensed data. *J. Geophys. Res.*, **117**, C08009, https://doi.org/10.1029/2011JC007659.

Rixen, M., J. M. Beckers, and J. T. Allen, 2001: Diagnosis of vertical velocities with the QG Omega equation: A relocation method to obtain pseudo-synoptic data sets. *Deep-Sea Res. I*, **48**, 1347–1373, https://doi.org/10.1016/S0967-0637(00)00085-6.

Roden, G. I., 1975: On North Pacific temperature, salinity, sound velocity and density fronts and their relation to the wind and energy flux fields. *J. Phys. Oceanogr.*, **5**, 557–571, https://doi.org/10.1175/1520-0485(1975)005<0557:ONPTSS>2.0.CO;2.

Rudnick, D. L., 1996: Intensive surveys of the Azores Front 2. Inferring the geostrophic and vertical velocity fields. *J. Geophys. Res.*, **101**, 16 291–16 303, https://doi.org/10.1029/96JC01144.

——, 2016: Ocean research enabled by underwater gliders. *Annu. Rev. Mar. Sci.*, **8**, 519–541, https://doi.org/10.1146/annurev-marine-122414-033913.

——, 2021: Observations of the Almeria–Oran Front in the Mediterranean Sea using Spray underwater gliders.

Instrument Development Group, Scripps Institution of Oceanography, accessed 30 March 2021, https://doi.org/10.21238/S8SPRAY3700.

——, and J. R. Luyten, 1996: Intensive surveys of the Azores Front 1. Tracers and dynamics. *J. Geophys. Res.*, **101**, 923–939, https://doi.org/10.1029/95JC02867.

——, and R. Ferrari, 1999: Compensation of horizontal temperature and salinity gradients in the ocean mixed layer. *Science*, **283**, 526–529, https://doi.org/10.1126/science.283.5401.526.

——, and J. Klinke, 2007: The underway conductivity-temperature-depth instrument. *J. Atmos. Oceanic Technol.*, **24**, 1910–1923, https://doi.org/10.1175/JTECH2100.1.

——, and S. T. Cole, 2011: On sampling the ocean using underwater gliders. *J. Geophys. Res.*, **116**, C08010, https://doi.org/10.1029/2010JC006849.

——, R. E. Davis, C. C. Eriksen, D. M. Fratantoni, and M. J. Perry, 2004: Underwater gliders for ocean research. *Mar. Technol. Soc. J.*, **38**, 73–84, https://doi.org/10.4031/002533204787522703.

——, ——, and J. T. Sherman, 2016: Spray underwater glider operations. *J. Atmos. Oceanic Technol.*, **33**, 1113–1122, https://doi.org/10.1175/JTECH-D-15-0252.1.

——, J. T. Sherman, and A. P. Wu, 2018: Depth-average velocity from Spray underwater gliders. *J. Atmos. Oceanic Technol.*, **35**, 1665–1673, https://doi.org/10.1175/JTECH-D-17-0200.1.

Sawyer, J. S., 1956: The vertical circulation at meteorological fronts and its relation to frontogenesis. *Proc. Roy. Soc. London*, **234A**, 346–362, https://doi.org/10.1098/rspa.1956.0039.

Schofield, O., and Coauthors, 2007: Slocum gliders: Robust and ready. *J. Field Rob.*, **24**, 473–485, https://doi.org/10.1002/rob.20200.

Sherman, J., R. E. Davis, W. B. Owens, and J. Valdes, 2001: The autonomous underwater glider "Spray." *IEEE J. Oceanic Eng.*, **26**, 437–446, https://doi.org/10.1109/48.972076.

Song, X. Z., and L. S. Yu, 2017: Air-sea heat flux climatologies in the Mediterranean Sea: Surface energy balance and its consistency with ocean heat storage. *J. Geophys. Res.*, **122**, 4068–4087, https://doi.org/10.1002/2016JC012254.

Tandon, A., E. A. D'Asaro, K. M. Stafford, D. Sengupta, M. Ravichandran, M. Baumgartner, R. Venkatesan, and T. Paluszkiewicz, 2016: Technological advancements in observing the upper ocean in the Bay of Bengal: Education and capacity building. *Oceanography*, **29**, 242–253, https://doi.org/10.5670/oceanog.2016.56.

Thomas, L. N., C. M. Lee, and Y. Yoshikawa, 2010: The subpolar front of the Japan/East Sea. Part II: Inverse method for determining the frontal vertical circulation. *J. Phys. Oceanogr.*, **40**, 3–25, https://doi.org/10.1175/2009JPO4018.1.

Tintoré, J., P. E. Laviolette, I. Blade, and A. Cruzado, 1988: A study of an intense density front in the eastern Alboran Sea: The Almeria–Oran Front. *J. Phys. Oceanogr.*, **18**, 1384–1397, https://doi.org/10.1175/1520-0485(1988)018<1384:ASOAID>2.0.CO;2.

——, D. Gomis, S. Alonso, and G. Parilla, 1991: Mesoscale dynamics and vertical motion in the Alborán Sea. *J. Phys. Oceanogr.*, **21**, 811–823, https://doi.org/10.1175/1520-0485(1991)021<0811:MDAVMI>2.0.CO;2.

Todd, R. E., D. L. Rudnick, J. T. Sherman, W. B. Owens, and L. George, 2017: Absolute velocity estimates from autonomous underwater gliders equipped with Doppler current profilers. *J. Atmos. Oceanic Technol.*, **34**, 309–333, https://doi.org/10.1175/JTECH-D-16-0156.1.

Viúdez, A., J. Tintoré, and R. L. Haney, 1996a: Circulation in the Alboran Sea as determined by quasi-synoptic hydrographic observations. 1. Three-dimensional structure of the two anticyclonic gyres. *J. Phys. Oceanogr.*, **26**, 684–705, https://doi.org/10.1175/1520-0485(1996)026<0684:CITASA>2.0.CO;2.

——, ——, and ——, 1996b: About the nature of the generalized omega equation. *J. Atmos. Sci.*, **53**, 787–795, https://doi.org/10.1175/1520-0469(1996)053<0787:ATNOTG>2.0.CO;2.

Zarokanellos, N. D., D. L. Rudnick, and J. Tintoré, 2021: SOCIB CALYPSO Glider Observations (Version 1.0.0). Balearic Islands Coastal Observing and Forecasting System, SOCIB, accessed 8 April 2021, https://doi.org/10.25704/QMZF-VV36.

——, ——, M. Garcia-Jove, B. Mourre, S. Ruiz, A. Pascual, and J. Tintoré, 2022: Frontal dynamics in the Alboran Sea—Part I: Coherent 3D pathways at the Almeria–Oran front using underwater glider observations. *J. Geophys. Res. Oceans*, https://doi.org/10.1029/2021JC017405, in press.